Lim et al. *EPJ Quantum Technology* (2017) 4:11
DOI 10.1140/epjqt/s40507-017-0064-x

EPJ Quantum Technology
a SpringerOpen Journal

EPJ.org

RESEARCH Open Access

Laser annealing heals radiation damage in avalanche photodiodes

Jin Gyu Lim[1,2*], Elena Anisimova[1,3], Brendon L Higgins[1,3], Jean-Philippe Bourgoin[1,3], Thomas Jennewein[1,3,4] and Vadim Makarov[3,1,2]

*Correspondence:
j29lim@uwaterloo.ca
[1]Institute for Quantum Computing, University of Waterloo, Waterloo, ON N2L 3G1, Canada
[2]Department of Electrical and Computer Engineering, University of Waterloo, Waterloo, ON N2L 3G1, Canada
Full list of author information is available at the end of the article

Abstract

Avalanche photodiodes (APDs) are a practical option for space-based quantum communications requiring single-photon detection. However, radiation damage to APDs significantly increases their dark count rates and thus reduces their useful lifetimes in orbit. We show that high-power laser annealing of irradiated APDs of three different models (Excelitas C30902SH, Excelitas SLiK, and Laser Components SAP500S2) heals the radiation damage and several APDs are restored to typical pre-radiation dark count rates. Of nine samples we test, six APDs were thermally annealed in a previous experiment as another solution to mitigate the radiation damage. Laser annealing reduces the dark count rates further in all samples with the maximum dark count rate reduction factor varying between 5.3 and 758 when operating at –80°C. This indicates that laser annealing is a more effective method than thermal annealing. The illumination power to reach these reduction factors ranges from 0.8 to 1.6 W. Other photon detection characteristics, such as photon detection efficiency, timing jitter, and afterpulsing probability, fluctuate but the overall performance of quantum communications should be largely unaffected by these variations. These results herald a promising method to extend the lifetime of a quantum satellite equipped with APDs.

Keywords: laser annealing; avalanche photodiodes; single-photon detectors; quantum communications

1 Introduction

Quantum communications protocols, such as quantum key distribution (QKD) [1, 2], quantum teleportation [3], and Bell's inequality tests [4], are limited to transmission distances of only a few hundred kilometers [5–7] under the restrictions of present technology. For global-scale quantum communications, quantum repeaters [8] and quantum satellites [9–11] are potential solutions. Unfortunately, quantum repeaters are not ready for deployment as quantum memories with sufficient storage times and fidelities, upon which quantum repeaters depend, are still being developed [12, 13]. On the other hand, quantum communications to satellite platforms are feasible today [14–22], with China being the first country to successfully launch a quantum satellite [23].

One of many challenges in achieving long-distance quantum communications is the noise floor imposed by detector dark counts [24] - false photon detection events caused by thermally excited, tunneling, and trapped electrons [25]. A previous study [26] examined

the performance of both downlink and uplink satellite quantum communication designs under various conditions. Uplink communication, where the detectors are placed on the satellite, is particularly interesting because of potentially simpler satellite designs and easy interchangeability of sources at the ground station - for this approach, QKD, quantum teleportation, and Bell tests perform well with a dark count rate up to about 200 Hz per detector.

Silicon avalanche photodiodes (APDs) are an appropriate choice for the single-photon detector on a satellite because of their low dark count rate, good sensitivity in 400-1,000 nm wavelength range (covering wavelengths near 785 nm for optimal uplink transmissions [26]), and no need for cryogenic cooling [27–29]. However, proton radiation in low Earth orbit significantly increases APD dark count rates over time [30–34]. In a recent experiment [35], APD samples (Excelitas C30902SH, Excelitas SLiK, and Laser Components SAP500S2) were irradiated by different fluences of 106 MeV protons to simulate radiation effects over 0.6, 6, 12, and 24 months in a representative low Earth polar orbit. There it was shown that thermal annealing of irradiated APDs at up to 100°C can repair some of the damage, resulting in up to 6.6-fold dark count rate reduction. A separate study showed that a certain power range of focused laser illumination can lower non-irradiated APD dark count rates by up to 5.4 times [36].

Here we perform laser annealing on nine irradiated APDs. We find that laser annealing successfully decreases the dark count rates in all nine irradiated APD samples by a factor ranging from 5.3 to 758 when operated at –80°C. We demonstrate dark count rate reductions due to laser annealing can exceed those from thermal annealing. Notably, we observe that dark count rates are reduced even when laser annealing is applied to APDs that were already thermally annealed. Laser annealing also affects other important photon counting parameters including photon detection efficiency, timing jitter, and afterpulsing probability, but the operation of quantum communications applications should not be significantly influenced by these changes.

2 Experimental setup

2.1 Test samples

We test the same Excelitas C30902SH, Excelitas SLiK, and Laser Components SAP500S2 devices used in the previous study [35]. These were chosen as they are the only commercially available thick-junction APD models (thick-junction APDs have higher detection efficiencies at the quantum signal wavelength around 785 nm, which makes them the most appealing for use on a quantum satellite receiver). All our APD samples are hermetically sealed in glass-window packages and the photosensitive areas of C30902SH and SAP500S2 are 500 μm in diameter, while that of SLiK is 180 μm in diameter. Table 1 presents the details of previous radiation testing and thermal annealing procedures performed on our test samples. These samples were stored in a –20°C freezer before our experiments to prevent any spontaneous annealing at room temperature.

For every detector, the dark count rate after irradiation (and any thermal annealing) is so high that the devices are saturated when operating at room temperature. For this reason, all samples are characterized at –80°C in our cold-temperature characterization apparatus. However, unlike the other devices, each Excelitas SLiK comes with a built-in thermistor and thermoelectric cooler (TEC), allowing additional testing to be performed in-situ in our laser annealing apparatus at an operating temperature of –30°C.

Table 1 Summary of detector samples, applied radiation, previous thermal annealing, and measured results of laser annealing

Sample ID	106 MeV proton fluence (cm^{-2})	Equivalent time in 600 km polar orbit (months)	Thermal annealing procedure	Dark count rate at –80°C				Annealing power (W)	V_{excess} (V)
				Before (Hz)	Lowest after (Hz)	Highest reduction factor	Typical for pre-radiation (Hz)		
C30902SH-1	10^9	6	None	347	2.3	150	~5	0.8	14
C30902SH-2	10^9	6	None	363	2.64	137	~5	1.5	14
SLiK-1	10^8	0.6	2 h @ +100°C	6.71	0.16	41.7	<1	1.4	14
SLiK-2	10^8	0.6	2 h @ +100°C	2.19	0.42	5.3	<1	0.8	14
SLiK-3	4×10^9	24	4 h @ +80°C, 2 h @ +100°C	43.1	2.09	21	<1	1.4	14
SLiK-4	10^9	6	None	192	8.3	23	<1	1.0	20
SLiK-5	4×10^9	24 (applied bias voltage)	3 h @ +80°C, 2 h @ +100°C	447	58	7.7	<1	1.0	20
SAP500S2-1	4×10^9	24	4 h @ +80°C, 2 h @ +100°C	1,579	2.08	758	~2	1.4	20
SAP500S2-2	10^8	0.6	2 h @ +100°C	213	1.66	128	~2	1.6	20

The detectors are referred to by the given sample IDs throughout the paper. The highest reduction factor is the ratio between the reference dark count rate before any laser annealing and the lowest dark count rate after laser annealing - the corresponding laser power for this is also given. We include typical pre-radiation dark count rates of each model under the same bias and temperature conditions [35, 37].

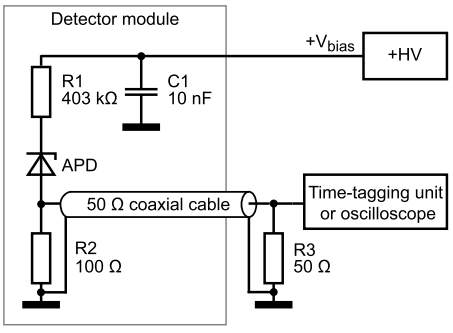

Figure 1 Detector module circuit. Each detector module houses a number of APDs (up to six), all of which were irradiated to a common fluence. The circuit diagram for a single detector channel is shown - each APD is embedded in passive avalanche quenching electronics with an external high-voltage supply and output to a time-tagging unit (the time-tagging unit has a fixed-threshold discriminator at each input) or to an oscilloscope.

The samples are held in detector modules, which are moved between the annealing and characterization apparatuses as necessary and provide avalanche detection and quenching. We employ a passive quenching circuit [25, 38] (see Figure 1) for processing output avalanche pulses. In this circuit, the APD is reverse-biased in Geiger-mode [25], where the bias voltage (V_{bias}) is set above the detector's breakdown voltage (V_{br}) and the APD becomes sensitive to single photons [38]. V_{excess} (= $V_{bias} - V_{br}$), typically ~20 V, generates a high electric field in the detector's depletion and avalanche regions. When a detection takes place (ideally, by a photon incident on the APD active area), an electron-hole pair is generated. The high electric field in the p-n junction causes impact ionization and produces an avalanche current flow. The current flow is detected as a voltage drop across R2 in parallel with a 50 Ω impedance coaxial cable. If this voltage drop is greater than a discriminator's fixed threshold voltage, a detection event is recorded. R1 quenches the current flow by lowering the voltage across the APD close to V_{br} [38]. Once the diode voltage reaches near V_{br} and the steady-state current flow (V_{excess}/R1) is below a latch current of

$\sim$100 μA, the avalanche current flow stops [38]. Our detector module has the steady-state current of $\approx$50 μA for V_{excess} = 20 V.

We measure the dark count rate, relative changes in photon detection efficiency (P_{de}) (and absolute P_{de} for SLiKs characterized at –30°C), and afterpulsing time distribution through the analysis of detection event times produced by a time-tagging unit with 156.25 ps resolution (UQDevices 16-channel model). Timing jitter (Δt_{jitter}) is measured using an oscilloscope (LeCroy 640Zi).

2.2 Laser annealing apparatus

Figure 2(a) shows the laser annealing apparatus, which improves upon the laser annealing experimental setup of Ref. [36]. Our apparatus allows us to laser-anneal APDs, take pictures of their active areas, measure their dark count rates and P_{de}, and scan P_{de} across the entire active area to check whether laser annealing has produced any local damage.

Our setup consists of a single-mode (SM) continuous-wave 808 nm signal laser (QPhotonics QFLD-808-100S), and one multi-mode (MM) 0-30 W continuous-wave 808 nm annealing laser LD2 (Jenoptik JOLD-30-FC-12). The 808 nm wavelength is selected for the annealing laser to ensure that APDs fully absorb photons in the depletion region and generate heat energy. Typical depletion region thickness of thick-junction silicon APDs is 20-150 μm [38]. At 300 K, if the wavelength is too long (>1,100 nm), the APDs transmit most photons. If the wavelength is too short (<500 nm), most photons are absorbed only at the surface of the APDs [39]. Absorption depth of 808 nm photons, at which the light intensity has fallen to 1/e of the initial value, is $\sim$10 μm [39]. The pigtail of the signal laser LD1 is connected to a 90:10 fiber beamsplitter (Thorlabs FC780-90B FC). One output port is connected to a power meter (PM1; OZ Optics POM-300-VIS), while the

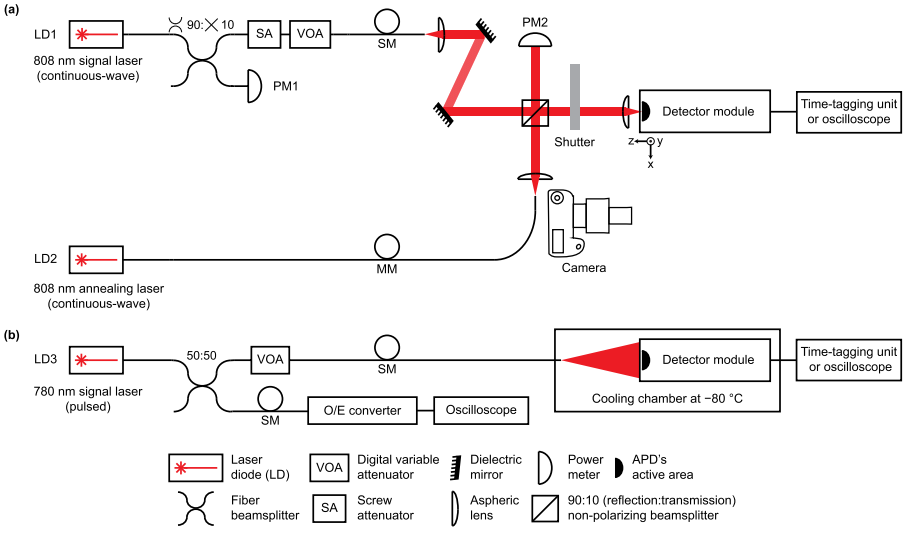

Figure 2 Experimental setup. (a) Setup for laser annealing and characterization at room temperature. (b) Setup for characterization at –80°**C**. In (a), LD1 and LD2 are overlapped such that high-power laser from LD2 can be focused on the APD's active area by focusing LD1 onto it. LD1 is also used for measuring SLiKs' photon detection efficiency. The detector module is mounted on an XYZ translation stage, which can move between the laser setup and camera. The free-space portion of the setup is enclosed in a light-tight box. In (b), diverging weak coherent pulses are applied on APDs for full characterization. SM: single-mode optic fiber; MM: multi-mode optic fiber; O/E: optical-to-electrical.

other output port is connected to two attenuators in series: a screw attenuator reduces laser power to the nW range, and a digital variable attenuator (OZ Optics DA-100-35-770/830/850-5/125-5-40-LL) then brings laser illumination down to the single-photon level. The degree of attenuation and the output power from the weak coherent continuous-wave light source are calibrated to apply the mean photon count rate of 48.8 kHz at the sample. The attenuated continuous-wave laser beam is sent to a collimation setup in SM fiber, then collimated by an aspheric lens (Thorlabs C280TME-B) and reflected off two dielectric mirrors (Thorlabs BB1-E03-10) to provide four degrees of freedom for alignment. It then goes through 90:10 (reflection:transmission) non-polarizing beamsplitter (Thorlabs BS029 90:10), a mechanical shutter (Thorlabs SH05 with Thorlabs SC10 controller), a focusing lens (Thorlabs C220TME-B), and reaches the APD.

The continuous-wave annealing laser LD2 is coupled to a 200 μm diameter core MM fiber (RPMC Lasers OAL-200/220/245). The annealing laser beam is collimated by an aspheric lens (Thorlabs C220TME-B) and reflected at the 90:10 non-polarizing beamsplitter. The beams of the annealing and signal lasers overlap so that both can be focused on the same spot. A power meter (PM2; Thorlabs S142C) located in the transmission arm of the annealing laser allows us to accurately control the annealing power at the APD.

A camera (Canon 7D with macro lens MP-E 65 mm f/2.8 1-5×) and a light-emitting-diode photography illuminator are mounted beside the laser setup. The XYZ translation stage, on which the detector module is mounted, enables us to move the samples between the laser setup and the camera.

2.3 Cold-temperature characterization apparatus

A separate apparatus, shown in Figure 2(b), is built to measure the dark count rate, relative changes in P_{de}, Δt_{jitter}, and afterpulsing probability at −80°C. The low temperature significantly suppresses thermally excited dark counts [35]. The detector module is extracted from the laser annealing apparatus and placed inside a cooling chamber (Delta Design 9023) at −80°C.

The apparatus necessary to measure the absolute P_{de} cannot fit in the cooling chamber; consequently, we measure P_{de} relative to a reference by sending diverging weak coherent pulses (WCPs) from the end of a fiber onto the APDs. Each APD's active area is sufficiently small that it receives approximately uniformly distributed light intensity, despite the overall Gaussian profile of the incident optical mode. We use a 780 nm laser LD3 (PicoQuant LDH 8-1) as the WCP source, pulsed at 40 MHz with full width at half maximum (FWHM) of 188 ps. The laser pulses are split by a 50:50 fiber beamsplitter (Thorlabs FC780-50B-FC). One output port is connected to a digital variable attenuator (OZ Optics DA-100-35-770/830/850-5/125-5-40-LL) and sends the laser pulses through a fiber to the APDs placed inside the cooling chamber. The other output port is connected to an optical-to-electrical converter (LeCroy OE455, DC-3.5 GHz) and the oscilloscope. Having oscilloscope access to both input laser pulses and output avalanche pulses allows us to measure Δt_{jitter} (which requires using a pulsed laser, as opposed to continuous-wave such as LD1).

3 Methods

3.1 Laser annealing

To perform laser annealing, the detector module is positioned to ensure that the high-power annealing laser beam is focused on the active area of an APD. (The FWHM beam

diameter is 92 μm.) Next, the desired annealing power is set by monitoring the power meter PM2 with the shutter closed. We then open the shutter and laser-anneal the APD for 60 s, immediately afterwards closing the shutter and letting the device cool down to the room temperature for another 60 s. We then perform characterization.

For most samples, we perform multiple stages of laser annealing and characterization, with laser power increased between each stage. To determine whether this stepwise laser annealing process has any additional effects, we apply only a single-shot power of 1 W to SLiK-4 and SLiK-5 for comparison (1 W is chosen based on observed results of the first three SLiKs to ensure a dark count rate reduction). Similarly, C30902SH-2 is laser-annealed at two specific powers, chosen based on C30902SH-1's observed results.

The temperatures reached by the APDs during laser annealing are of interest because, for some temperature ranges, alternative heating methods may be more practical to implement on a satellite (e.g., using an electric heater). We can measure the temperature of SLiK samples using their integrated thermistor (mounted on the cold plate of TEC, close to the APD). The temperature of SLiK-1's thermistor is recorded at the end of the 60 s exposure, for most annealing powers. According to our measurements (see Appendix), the thermal resistance between the photodiode chip and thermistor is negligible; thus, the temperature reading by the thermistor provides an accurate reading of the temperature reached by the APD during laser annealing.

3.2 Characterization

All nine samples' parameters are measured at −80°C in the cold-temperature characterization apparatus, while SLiKs are also characterized at −30°C (reached using their built-in TECs) in the laser annealing apparatus.

Breakdown voltage. We measure V_{br} by observing avalanche pulses on an oscilloscope. As V_{bias} is gradually increased from 0 V, avalanche pulses begin to appear when V_{br} is reached. We estimate the accuracy of this V_{br} measurement to be better than $\pm$0.3 V. This measurement is performed at the start of every full characterization. Both C30902SH samples and SLiK-1, SLiK-2, and SLiK-3 are subsequently biased +14 V above V_{br}, whereas SLiK-4, SLiK-5, and both SAP500S2 samples are biased +20 V above V_{br}. The choice of V_{excess} is arbitrary; however, we change V_{excess} values to explore its effects on laser-annealed APDs.

Dark count rate. We record dark counts with the time-tagging unit for 500 s. The mean dark count rate is calculated from the collected time-stamped data. We define the dark count rate reduction factor as the ratio between the reference mean dark count rate before any laser annealing and the mean dark count rate after laser annealing. Some of the samples were already thermally annealed in another experiment [35]; thus, having further dark count rate reduction in those samples imply that laser annealing mitigates proton radiation damage better than thermal annealing.

Photon detection efficiency. To measure relative P_{de} at −80°C in the cold-temperature characterization apparatus using diverging WCPs, we take the mean count rate over 500 s. Following the completion of laser annealing and measurements of the two C30902SH samples, it was discovered that the output power of LD3 varies over time. As the C30902SH samples have undergone laser annealing, measurements unfortunately cannot be retaken. Consequently, for all other samples, we normalize the count rate by the

average laser power (measured at the oscilloscope immediately before and after a measurement). We then calculate the relative change in P_{de} by subtracting the mean dark count rate and then normalizing against the initial photon count rate.

For SLiKs we determine the absolute P_{de} while operating at –30°C in the laser annealing apparatus. The continuous-wave signal laser LD1 is applied, with its photon rate calibrated via loss and laser power measurements in our optical setup. Then, we measure a mean count rate over 500 s using the time-tagging unit. Subtracting the mean dark count rate from the mean count rate and dividing the difference by the calibrated input photon rate gives P_{de}.

Testing within the laser annealing apparatus also allows us to scan P_{de} at various points over the active area of the SLiK devices. We measure the signal laser's illumination spot size using a beam profiler - the beam waist is ∼20 μm (FWHM). We thus step the translation stages in 10 μm increments, such that P_{de} of the active area is fully and tightly covered. We scan a square region that covers the active area, with appropriate pauses at each step for vibration dissipation.

Timing jitter. To measure Δt_{jitter}, both the laser output pulses and the APD's avalanche pulses are connected to the oscilloscope. We then plot a histogram of the relative time difference between these two signals over at least 10^5 avalanche pulses (see example in Figure 3), and measure the FWHM.

Afterpulsing probability. Afterpulsing probability is calculated from time-stamped counts. We typically use dark counts, but if the dark count rate for an APD is too low, we use a dim light pulsed at 100 Hz to facilitate a measurement. The extra light increases the background count rate by a few Hz (otherwise, the background count rate tracks the APD's dark count rate), and does not influence the afterpulsing distribution.

For every detection event, our software adds all subsequent detection events occurring up to 10^{-2} s later to a histogram, with exponentially growing time bins [37], as shown in Figure 4. Unlike the standard autocorrelation method, this improved analysis produces a plot that converges to the background count rate, instead of following an exponential decay. Using exponentially increasing bin sizes filters out statistical fluctuations in the tail and also resolves the fast changing avalanche peak.

The shape of this histogram (Figure 4) presents four features: an APD's dead time, its recharge time, its trapped-electron time constants, and the background count rate. In Figure 4, the dead time begins immediately after a photon detection (time 0) and ends when counts begin to reappear at roughly 0.8 μs. The recharge time is the time it takes for the

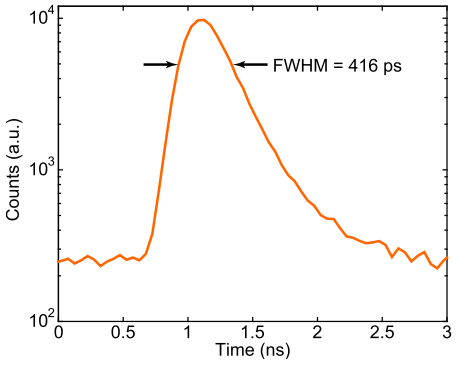

Figure 3 Timing jitter of SAP500S2-2. We measure the relative time difference between laser pulses and APD output pulses over at least 10^5 output pulses, and plot these as a histogram. Δt_{jitter} is the width of the pulse peak.

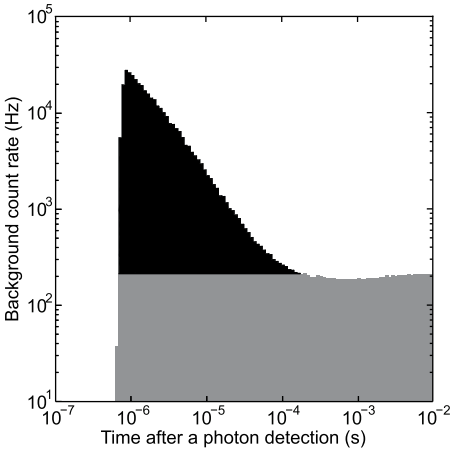

Figure 4 Afterpulsing histogram of SAP500S2-2. The histogram of the time difference between APD output pulses shows the APD's dead time from 0 to roughly 0.8 μs, followed by a recharge time of ≈150 ns. The following peak is formed of afterpulses. The count rates then settle down to the background count rate of ≈200 Hz. A possible reason for a slight increase in the count rate at the end is the high voltage supply rebounding after being slightly sagged by the charge being drawn by the single avalanche. The black shaded area is the afterpulsing probability.

count rate to reach the peak value after the dead time. Trapping time constants can be found by fitting the exponentially decaying slope of the peak. The plot levels off to the background count rate and the black shaded area is the afterpulsing probability.

For a quantum communications protocol such as QKD, the afterpulsing peak contributes to the quantum bit error rate (QBER), and it is thus desirable to remove the peak by extending the dead time out to the flattened region [28, 29, 38]. In practice, this can be performed by discarding all counts before the end of a user-selected dead time in post-processing [40, 41] or by using an active quenching circuit [42]. Such additional dead time, however, limits the maximum detection rate [27, 28]. Because long distance transmissions reduce the expected detection rate [43], the amount of additional dead time could be optimized to balance the QBER with the detection rate to maximize the final key rate [37, 40, 41].

4 Results and discussion

Right half of Table 1 summarizes the laser annealing results for the maximum dark count rate reduction. Detailed results for each APD model follow.

Excelitas SLiK. Figure 5 shows characterization results for the five SLiKs. The maximum dark count rate reduction ranges from 1.3 to 10 times when operating at –30°C, and from 5.3 to 41.7 times at –80°C. Importantly, the SLiKs that were previously thermally annealed exhibit further dark count rate reduction after laser annealing. SLiK-4 and SLiK-5, after a single exposure at 1 W, still show a significant decrease in the dark count rate. 1 W may not give the highest reduction factor but it shows that the single exposure and stepwise annealing processes induce comparable dark count rate reduction factors. Thus, the stepwise process can be used on a SLiK to find the optimal annealing power and a single exposure at this power on other SLiKs under similar conditions should achieve comparable dark count rate reduction.

P_{de} of each SLiK did not change significantly, and a spatial scan in Figure 6 shows that photosensitivity across the active area is not altered by high-power laser annealing. V_{br} and Δt_{jitter} also do not fluctuate much after laser annealing. SLiK-4's and SLiK-5's Δt_{jitter} are lower than those of other SLiKs due to the 6 V difference in V_{excess} [38].

The afterpulsing probability results are interesting. Proton radiation mainly causes displacement damage in APDs [44]. Highly energetic protons displace atoms from their lat-

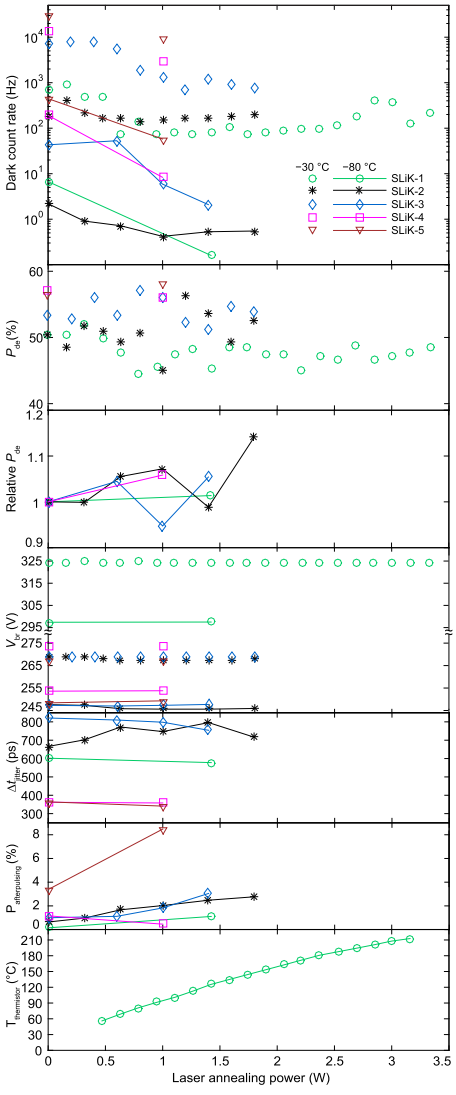

Figure 5 Characteristics of SLiK APDs after laser annealing. Points at zero power show the initial characteristics before laser annealing. The samples have been characterized at −30°C after every annealing stage (data represented by points without lines), and additionally characterized at −80°C after some of the steps (points connected with lines).

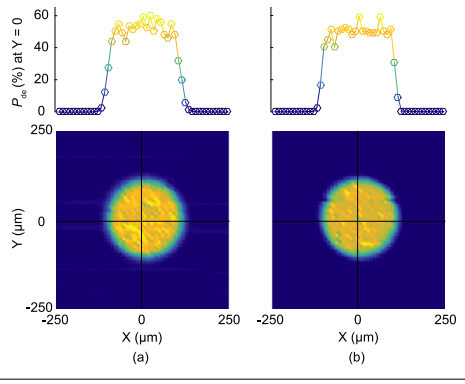

Figure 6 Detection efficiency scan of SLiK-1. (a) Prior to annealing, and (b) after 3.3 W annealing. The spatial profile is essentially unchanged, proving that focused high-power laser illumination does not degrade photosensitivity in the active region of the APD for the power range we tested. The plots at the top are the cross sections at $Y = 0$.

tice structures, producing extra energy levels in the bandgap (defects). The defects near the mid-bandgap contribute to thermally generated dark counts, while those near the conduction band are called trap levels that cause afterpulses. After proton irradiation, SLiKs'

dark count rates are significantly increased but the afterpulsing probabilities are still low [35], implying that the displacement damage by 106 MeV protons at the depletion region mainly produces thermal generation centers [44]. Although the dark count rate is reduced in all samples after laser annealing, the afterpulsing probability increases in most of them. This also implies that laser annealing not only removes thermal generation centers but also simultaneously creates extra trap levels. The increased afterpulsing probability can be handled by imposing additional dead time (see Section 3.2).

When the high-power laser is applied to SLiK-1, its thermistor temperature rapidly increases in the first 30 s. The temperature continues to rise at a slower rate in the second half of the 60 s exposure until it reaches the peak temperature in the last 2-3 s. The peak thermistor temperature at each annealing power is plotted in Figure 5. The SLiKs we have tested experience a significant dark count rate reduction at annealing power of 1 W. Assuming the thermal resistance between SLiK-1's thermistor and the APD is negligible (see Appendix), 1 W of power anneals the APD at peak temperature of ∼90°C. The peak temperature is reached only in the last few seconds, but we speculate that it determines the dark count rate reduction factor. If this is the case, our results imply that laser-annealing irradiated SLiKs at the peak temperature of ∼90°C for 60 s leads to a higher dark count rate reduction than thermally annealing them at 100°C for two hours [35] (see Table 1). The observed discrepancy in the dark count rate reduction suggests that light may play a greater role than simply providing the heat energy in improving irradiated SLiKs' performance.

For SLiK-1, we continue to test at higher powers. Figure 7 shows the gradual change in the appearance of SLiK-1's active area. Figure 7(a) does not show any visible physical destruction, but the device has already stopped working as a single-photon detector after annealing at 3.5 W. In Figure 7(b)-(d), damage becomes visible. It appears that an epoxy layer between two ceramic plates has boiled and condensed on the package window, causing it to become opaque. We did not remove the blurry detector window because it may change illumination power calibration and cause oxidation due to exposure of the hermetically

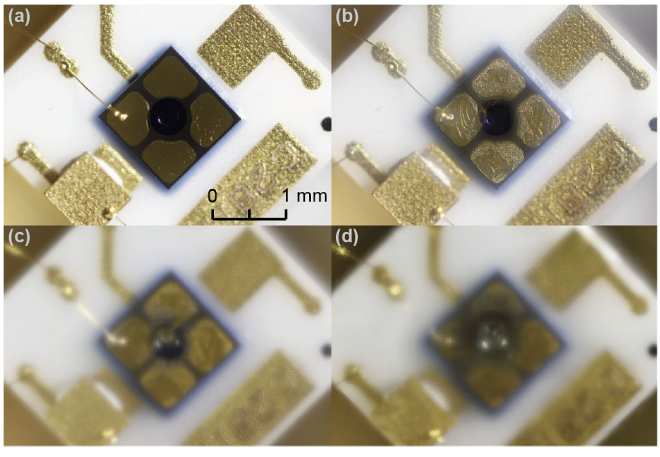

Figure 7 Progressive destruction of SLiK-1. The sample is exposed to laser power of (a) 3.5 W, (b) 5.2 W, (c) 7.7 W, and (d) 9.0 W. The photodiode stopped working as a single-photon detector after annealing at 3.5 W. From 3.6 W, the gold plating surrounding the active area of the APD begins to degrade and flow into the active area at higher powers. The package window becomes foggy from 4.9 W. The APD chip starts shifting downwards from 6 W and has moved by ≈ 30 μm overall.

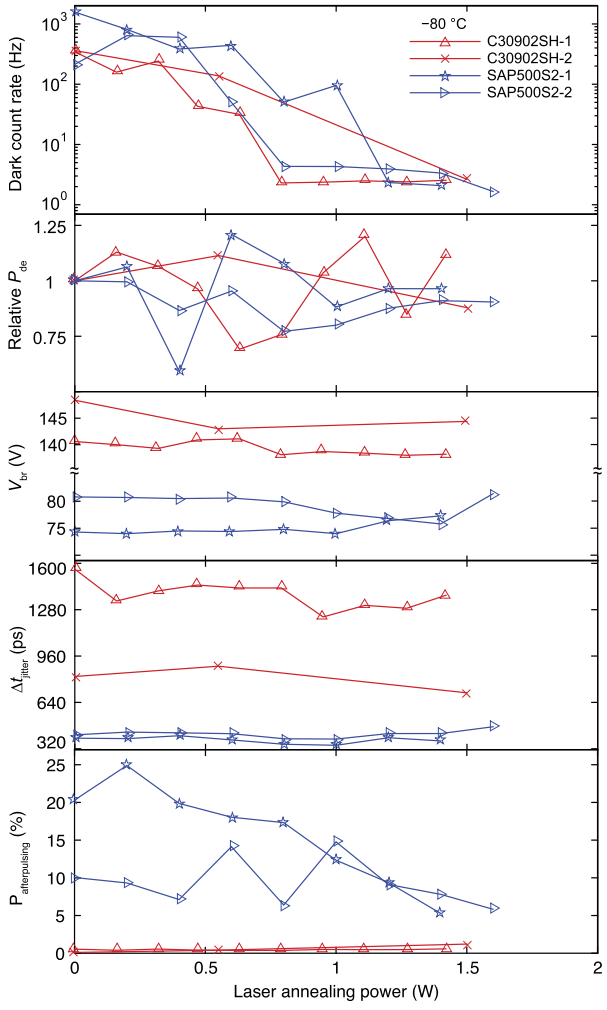

Figure 8 Characteristics of C30902SH and SAP500S2 APDs after laser annealing. Points at zero power show the initial characteristics before laser annealing. Each point shows a measurement after successive laser illumination power.

sealed package (filled with nitrogen gas) to the atmosphere. (SLiK's detailed mechanical structure can be seen in Figure 5 of Ref. [45]. Clear images of C30902SH's physical destruction are shown in Figure 4 of Ref. [36].)

Excelitas C30902SH. Figure 8 shows characterization results for the two irradiated C30902SHs. Similar to the SLiKs, C30902SH-1 is laser-annealed and characterized at multiple stages, but C30902SH-2 is treated at two specific powers, chosen based on C30902SH-1's results. The samples experience the maximum dark count rate reduction of 150 times and 137 times at –80°C. They recover typical pre-radiation dark count rates. Again, the stepwise process does not show any additional improvements on the dark count rate when compared to the single exposure process.

Relative P_{de} measurement for C30902SHs is inaccurate due to the fluctuation of the laser output power (which we normalize out for measurements of the other devices; see Section 3.2). Due to the variation observed, it is difficult to draw any conclusions. V_{br} and Δt_{jitter} do not change significantly. Afterpulsing probabilities are negligible in C30902SHs,

which also implies that thermal generation centers are the main contributors to dark counts after irradiation. We stop testing these C30902SHs before they show signs of damage - testing non-irradiated C30902SHs at higher powers was done in Ref. [36].

Laser Components SAP500S2. Unlike SLiKs, SAP500S2s cannot withstand high-power illumination. SAP500S2-1 and SAP500S2-2 fail to work as single-photon detectors after laser annealing at 1.6 W and 1.8 W, respectively. Both SAP500S2s (see Figure 8) exhibit the maximum dark count rate reduction just before they stop working as a single-photon detector (the reduction factor of 758 times for SAP500S2-1 and 128 times for SAP500S2-2). SAP500S2s have the highest dark count rate after proton irradiation [35] and such high reduction factors prove that laser annealing is more effective than thermal annealing. The lowest dark count rates after laser annealing ($\approx$2 Hz) are at typical pre-radiation values.

Relative P_{de} varies for different laser annealing powers. Unlike C30902SH measurements, the photon count rate here is normalized to the laser source's average power for every characterization, so the observed variation is real. To avoid P_{de} fluctuation and achieve sufficiently low dark count rate, one should perform laser annealing around 1 W.

V_{br} seems to decrease slightly, and then increase just before each SAP500S2 stops working as a single-photon detector. An increase in V_{br} may be an indication that the maximum laser annealing power is reached. Δt_{jitter} remains almost constant and it is low compared to C30902SHs because SAP500S2s are biased an extra 6 V (for a V_{excess} = 20 V) above a significantly lower V_{br}.

While SLiKs and C30902SHs display a marginal increase in afterpulsing probability as the laser power increases, the afterpulsing probability is reduced in SAP500S2s (afterpulsing probability did not change much after proton irradiation [35]). Although these reductions are insignificant compared to the highest dark count rate reduction factor in Table 1, the results imply that laser annealing reduces both trap levels and thermal generation centers at the same time. The overall results suggest that the materials used to manufacture SAP500S2s are more susceptible to the high energy damages induced by protons and the annealing laser.

Although high-power laser exposure can be helpful for reducing APD dark counts, it also has the potential to damage components, such as classical photodiodes and pinholes, in quantum communication systems [46]. Such changes to the apparatus may invalidate assumptions - most notably, within the security analysis for implementations of QKD, which could lead to exploitable side-channels. However, having a reduction in dark counts does not benefit the eavesdropper because QKD security proofs attribute all losses and errors to the eavesdropper while assuming Bob's apparatus to be error-free [24].

The laser annealing apparatus could be reduced in complexity for implementation as part of a satellite payload; however, a high-power laser is still required. Further research is needed to understand the physical phenomena behind the dark count rate reduction, and determine whether the specific properties of laser light are fundamentally necessary to achieve the gains observed here.

5 Conclusion

Our results demonstrate that laser annealing can remedy simulated low Earth orbit radiation damage for three different types of APDs. The dark count rate of all samples, including the samples that were previously thermally annealed, is greatly reduced. Several of them have their dark count rates recovered to typical pre-radiation levels. This suggests

that laser annealing is a more effective method. The observed fluctuations in other photon counting parameters should not degrade the performance of quantum communication applications. We speculate that laser annealing heals crystal lattice structure defects, thermal generation centers in particular, created by proton radiation. By employing this effect, the lifespan of a quantum satellite may be lengthened.

Appendix: laser annealing temperature measurement

We measure the thermal resistance between the APD and the thermistor of SLiK-2, in order to estimate temperatures achieved by laser annealing. The thermistor mounted on the cold plate of the TEC (see Figure 5 in Ref. [45]) allows us to measure the cold plate's temperature during the laser annealing process. Thus, by finding the thermal resistance between the APD and the cold plate, we can predict the actual temperature produced by each annealing power.

Alternatively, measuring V_{br} provides an indirect measure of an APD's temperature. This method is convenient because we can easily measure V_{br} with the experimental setup. Before measurements, we find the relationship between V_{br} and temperature by setting the TEC controller to temperatures from –30°C to +20°C in 10°C increments and measuring V_{br} at each point. The fit line in Figure 9 shows that V_{br} linearly depends on temperature.

For the thermal resistance measurement, we turn off the TEC current but keep measuring thermistor temperature. We also vary the bias voltage over the range of 50 V to 90 V above V_{br} at room temperature. Such high bias voltages cause a high dark count rate, resulting in a constant current flow in the circuit. Consequently, the voltage across the APD is approximately V_{br} because of continuous quenching process, and V_{br} increases at high bias voltages owing to higher heat dissipation. When applying each bias voltage, we wait for the thermistor temperature to stabilize, and measure the voltage across the 1 kΩ readout resistor in the passive quenching circuit (replacing R2 in Figure 1 for more accurate avalanche current measurement). From this voltage value, we deduce V_{br} and the APD's power dissipation. Power dissipation of the APD is calculated by multiplying the avalanche current (on the order of a few hundred μA) and V_{br}. Using the linear relationship found in Figure 9, we find the APD's temperature and compare it to the thermistor temperature. The temperature difference divided by the APD's power dissipation gives us the thermal resistance. Table 2 summarizes thermal resistance test results. Although the results are somewhat noisy, making it difficult to find the exact thermal resistance, it is clear that

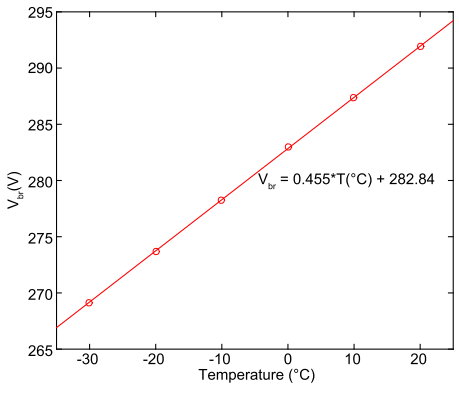

Figure 9 Breakdown voltage (V_{br}) of SLiK-2 at various temperatures. The relationship between V_{br} and temperature is linear. The coefficient of determination, R^2, is 0.99994.

Table 2 Measurement of thermal resistance between APD and cold plate

V_{bias} (V)	V_{br} (V)	ΔT (°C)	Power dissipation (mW)	Thermal resistance (K/W)
340	294.65	–0.16	33.4	–4.8
350	295.05	–0.44	40.5	–10.8
360	295.82	0.11	47.4	2.3
370	296.74	0.98	54.3	18.0
380	297.10	0.54	61.5	8.8

the thermal resistance is sufficiently small that the thermistor temperature approximately matches that of the APD itself. This assumption is used to estimate laser annealing temperature in conjunction with SLiK-1's thermistor temperature measurements during laser annealing procedure.

Acknowledgements
We thank those authors of Ref. [35] not listed in the present paper, namely M Cranmer, E Choi, D Hudson, LP Piche, and A Scott, for assisting with the detector sample irradiation campaign. We thank Excelitas for discussions and for providing selected APD samples. We thank T Graham and P Kwiat for an independent experimental confirmation of the laser annealing effect on an irradiated APD. This work was supported by the Canadian Space Agency, Industry Canada, CFI, NSERC (programs Discovery and CryptoWorks21), Ontario MRI, and the U.S. Office of Naval Research.

Abbreviations
APD: Avalanche Photodiodes; QKD: Quantum Key Distribution; TEC: Thermoelectric Cooler; PM: Power Meter; SM: Single-Mode; MM: Multi-Mode; WCP: Weak Coherent Pulse; FWHM: Full Width at Half Maximum; QBER: Quantum Bit Error Rate; VOA: Variable Optical Attenuator; SA: Screw Attenuator; O/E: Optical-to-Electrical; LD: Laser Diode.

Competing interests
The authors declare that they have no competing interests.

Authors' contributions
JGL performed the experiments, conducted data analysis, and wrote the manuscript with contributions from all authors. EA, BLH, JPB, TJ, and VM provided the samples and assisted with experimental setup and data analysis. TJ and VM supervised the study. All authors read and approved the final manuscript.

Author details
[1]Institute for Quantum Computing, University of Waterloo, Waterloo, ON N2L 3G1, Canada. [2]Department of Electrical and Computer Engineering, University of Waterloo, Waterloo, ON N2L 3G1, Canada. [3]Department of Physics and Astronomy, University of Waterloo, Waterloo, ON N2L 3G1, Canada. [4]Quantum Information Science Program, Canadian Institute for Advanced Research, Toronto, ON M5G 1Z8, Canada.

Publisher's Note

Received: 31 January 2017 Accepted: 29 May 2017 Published online: 07 June 2017

References

1. Bennett CH, Brassard G. Quantum cryptography: public key distribution and coin tossing. In: Proceedings of IEEE international conference on computers, systems, and signal processing. New York: IEEE Press; 1984. p. 175-9.
2. Ekert AK. Quantum cryptography based on Bell's theorem. Phys Rev Lett. 1991;67(6):661-3. doi:10.1103/PhysRevLett.67.661.
3. Bennett CH, Brassard G, Crépeau C, Jozsa R, Peres A, Wootters WK. Teleporting an unknown quantum state via dual classical and Einstein-Podolsky-Rosen channels. Phys Rev Lett. 1993;70:1895-9. doi:10.1103/PhysRevLett.70.1895.
4. Bell JS. On the Einstein Podolsky Rosen paradox. Physics. 1964;1:195-200.
5. Yin H-L, Chen T-Y, Yu Z-W, Liu H, You L-X, Zhou Y-H, Chen S-J, Mao Y, Huang M-Q, Zhang W-J, Chen H, Li MJ, Nolan D, Zhou F, Jiang X, Wang Z, Zhang Q, Wang X-B, Pan J-W. Measurement-device-independent quantum key distribution over a 404 km optical fiber. Phys Rev Lett. 2016;117:190501. doi:10.1103/PhysRevLett.117.190501.
6. Ma X-S, Herbst T, Scheidl T, Wang D, Kropatschek S, Naylor W, Wittmann B, Mech A, Kofler J, Anisimova E, Makarov V, Jennewein T, Ursin R, Zeilinger A. Quantum teleportation over 143 kilometres using active feed-forward. Nature. 2012;489:269-73. doi:10.1038/nature11472.
7. Scheidl T, Ursin R, Kofler J, Ramelow S, Ma X-S, Herbst T, Ratschbacher L, Fedrizzi A, Langford NK, Jennewein T, Zeilinger A. Violation of local realism with freedom of choice. Proc Natl Acad Sci USA. 2010;107(46):19708-13. doi:10.1073/pnas.1002780107.
8. Briegel H-J, Dür W, Cirac JI, Zoller P. Quantum repeaters: the role of imperfect local operations in quantum communication. Phys Rev Lett. 1998;81(26):5932-5. doi:10.1103/PhysRevLett.81.5932.

9. Buttler WT, Hughes RJ, Kwiat PG, Lamoreaux SK, Luther GG, Morgan GL, Nordholt JE, Peterson CG, Simmons CM. Practical free-space quantum key distribution over 1 km. Phys Rev Lett. 1998;81:3283. doi:10.1103/PhysRevLett.81.3283.
10. Rarity JG, Tapster PR, Gorman PM, Knight P. Ground to satellite secure key exchange using quantum cryptography. New J Phys. 2002;4(1):82. doi:10.1088/1367-2630/4/1/382.
11. Aspelmeyer M, Jennewein T, Pfennigbauer M, Leeb WR, Zeilinger A. Long-distance quantum communication with entangled photons using satellites. IEEE J Sel Top Quantum Electron. 2003;9(6):1541-51. doi:10.1109/JSTQE.2003.820918.
12. Simon C, Afzelius M, Appel J, Boyer de la Giroday A, Dewhurst SJ, Gisin N, Hu CY, Jelezko F, Kröll S, Müller JH, Nunn J, Polzik ES, Rarity JG, de Riedmatten H, Rosenfeld W, Shields AJ, Sköld N, Stevenson RM, Thew R, Walmsley IA, Weber MC, Weinfurter H, Wrachtrup J, Young RJ. Quantum memories. Eur Phys J D. 2010;58(1):1-22. doi:10.1140/epjd/e2010-00103-y.
13. Sangouard N, Simon C, de Riedmatten H, Gisin N. Quantum repeaters based on atomic ensembles and linear optics. Rev Mod Phys. 2011;83(1):33-80. doi:10.1103/RevModPhys.83.33.
14. Gilbert G, Hamrick M. Practical quantum cryptography: a comprehensive analysis (part one). Tech. Rep. MTR00W0000052. The MITRE Corporation; 2000.
15. Bonato C, Tomaello A, Da Deppo V, Naletto G, Villoresi P. Feasibility of satellite quantum key distribution. New J Phys. 2009;11(4):045017. doi:10.1088/1367-2630/11/4/045017.
16. Ursin R, Jennewein T, Kofler J, Perdigues JM, Cacciapuoti L, de Matos CJ, Aspelmeyer M, Valencia A, Scheidl T, Acin A, Barbieri C, Bianco G, Brukner C, Capmany J, Cova S, Giggenbach D, Leeb W, Hadfield RH, Laflamme R, Lütkenhaus N, Milburn G, Peev M, Ralph T, Rarity J, Renner R, Samain E, Solomos N, Tittel W, Torres JP, Toyoshima M, Ortigosa-Blanch A, Pruneri V, Villoresi P, Walmsley I, Weihs G, Weinfurter H, Zukowski M, Zeilinger A. Space-quest, experiments with quantum entanglement in space. Europhys News. 2009;40(3):26-9. doi:10.1051/epn/2009503.
17. Meyer-Scott E, Yan Z, MacDonald A, Bourgoin J-P, Hübel H, Jennewein T. How to implement decoy-state quantum key distribution for a satellite uplink with 50-dB channel loss. Phys Rev A. 2011;84:062326. doi:10.1103/PhysRevA.84.062326.
18. Xin H. Chinese academy takes space under its wing. Science. 2011;332(6032):904. doi:10.1126/science.332.6032.904.
19. Nordholt JE, Hughes RJ, Morgan GL, Peterson CG, Wipf CC. Present and future free-space quantum key distribution. In: Proc. of SPIE on free-space laser communication technologies. vol. 4635. 2002. p. 116-26. doi:10.1117/12.464085.
20. Takenaka H, Toyoshima M, Takayama Y, Koyama Y, Akioka M. Experiment plan for a small optical transponder onboard a 50 kg-class small satellite. In: Int. conf. on space optical systems and applications. 2011. p. 113-6. doi:10.1109/ICSOS.2011.5783653.
21. Higgins BL, Bourgoin J-P, Gigov N, Meyer-Scott E, Yan Z, Jennewein T. Detailed performance analysis of the proposed QEYSSAT quantum receiver satellite. In: Conf. on lasers and electro-optics JW4A.118. 2012. doi:10.1364/CLEO_AT.2012.JW4A.118.
22. Vallone G, Bacco D, Dequal D, Gaiarin S, Luceri V, Bianco G, Villoresi P. Experimental satellite quantum communications. Phys Rev Lett. 2015;115:040502. doi:10.1103/PhysRevLett.115.040502.
23. Gibney E. Chinese satellite is one giant step for the quantum Internet. Nature. 2016;535:478-9. doi:10.1038/535478a.
24. Scarani V, Bechmann-Pasquinucci H, Cerf NJ, Dušek M, Lütkenhaus N, Peev M. The security of practical quantum key distribution. Rev Mod Phys. 2009;81(3):1301-50. doi:10.1103/RevModPhys.81.1301.
25. Haitz RH. Mechanisms contributing to the noise pulse rate of avalanche diodes. J Appl Phys. 1965;36:3123-31. doi:10.1063/1.1702936.
26. Bourgoin J-P, Meyer-Scott E, Higgins BL, Helou B, Erven C, Hübel H, Kumar B, Hudson D, D'Souza I, Girard R, Laflamme R, Jennewein T. A comprehensive design and performance analysis of low Earth orbit satellite quantum communication. New J Phys. 2013;15:023006. doi:10.1088/1367-2630/15/2/023006.
27. Cova S, Ghioni M, Lotito A, Rech I, Zappa F. Evolution and prospects for single-photon avalanche diodes and quenching circuits. J Mod Opt. 2004;51(9):1267-88. doi:10.1080/09500340408235272.
28. Hadfield RH. Single-photon detectors for optical quantum information applications. Nat Photonics. 2009;3:696-705. doi:10.1038/nphoton.2009.230.
29. Eisaman MD, Fan J, Migdall A, Polyakov SV. Invited review article: single-photon sources and detectors. Rev Sci Instrum. 2011;82(7):071101. doi:10.1063/1.3610677.
30. Sun X, Reusser D, Dautet H, Abshire JB. Measurement of proton radiation damage to Si avalanche photodiodes. IEEE Trans Electron Devices. 1997;44(12):2160-6. doi:10.1109/16.644630.
31. Sun X, Dautet H. Proton radiation damage of Si APD single photon counters. In: Proceedings of radiation effects data workshop, IEEE. 2001. p. 146-50. doi:10.1109/REDW.2001.960462.
32. Sun X, Krainak MA, Abshire JB, Spinhirne JD, Trottier C, Davies M, Dautet H, Allan GR, Lukemire AT, Vandiver JC. Space-qualified silicon avalanche-photodiode single-photon-counting modules. J Mod Opt. 2004;51(9-10):1333-50. doi:10.1080/09500340408235276.
33. Tan YC, Chandrasekara R, Cheng C, Ling A. Silicon avalanche photodiode operation and lifetime analysis for small satellites. Opt Express. 2013;21:16946. doi:10.1364/OE.21.016946.
34. Tang Z, Chandrasekara R, Tan YC, Cheng C, Sha L, Hiang GC, Oi DKL, Ling A. Generation and analysis of correlated pairs of photons aboard a nanosatellite. Phys Rev Appl. 2016;5:054022. doi:10.1103/PhysRevApplied.5.054022.
35. Anisimova E, Higgins BL, Bourgoin J-P, Cranmer M, Choi E, Hudson D, Piche LP, Scott A, Makarov V, Jennewein T. Mitigating radiation damage of single photon detectors for space applications. EPJ Quantum Technol. 2017;4:10. doi:10.1140/epjqt/s40507-017-0062-z.
36. Bugge AN, Sauge S, Ghazali AMM, Skaar J, Lydersen L, Makarov V. Laser damage helps the eavesdropper in quantum cryptography. Phys Rev Lett. 2014;112:070503. doi:10.1103/PhysRevLett.112.070503.
37. Anisimova E, Nikulov D, Hu SS, Bourgon M, Ursin R, Jennewein T, Makarov V. Low-noise single-photon detector for long-distance free-space quantum communication. 2015. (Presented at Qcrypt 2015, Tokyo, Japan); manuscript in preparation.
38. Cova S, Ghioni M, Lacaita A, Samori C, Zappa F. Avalanche photodiodes and quenching circuits for single-photon detection. Appl Opt. 1996;35(12):1956-76. doi:10.1364/ao.35.001956.

39. Green MA, Keevers MJ. Optical properties of intrinsic silicon at 300 K. Prog Photovolt. 1995;3:189-92. doi:10.1002/pip.4670030303.
40. Yoshizawa A, Kaji R, Tsuchida H. A method of discarding after-pulses in single-photon detection for quantum key distribution. Jpn J Appl Phys. 2002;41(10):6016-7. doi:10.1143/JJAP.41.6016.
41. Yoshizawa A, Kaji R, Tsuchida H. After-pulse-discarding in single-photon detection to reduce bit errors in quantum key distribution. Opt Express. 2003;11(11):1303-9. doi:10.1364/OE.11.001303.
42. Sultana N, Jennewein T. A novel readout system for free-running negative feedback avalanche diodes to significantly suppress afterpulsing effect. 2016. (Presented at Qcrypt 2016, Washington, D.C., U.S.A.); manuscript in preparation.
43. Bourgoin J-P, Gigov N, Higgins BL, Yan Z, Meyer-Scott E, Khandani AK, Lütkenhaus N, Jennewein T. Experimental quantum key distribution with simulated ground-to-satellite photon losses and processing limitations. Phys Rev A. 2015;92:052339. doi:10.1103/PhysRevA.92.052339.
44. Srour JR, McGarrity JM. Radiation effects on microelectronics in space. Proc IEEE. 1988;76(11):1443-69. doi:10.1109/5.90114.
45. Sauge S, Lydersen L, Anisimov A, Skaar J, Makarov V. Controlling an actively-quenched single photon detector with bright light. Opt Express. 2011;19:23590-600. doi:10.1364/OE.19.023590.
46. Makarov V, Bourgoin J-P, Chaiwongkhot P, Gagné M, Jennewein T, Kaiser S, Kashyap R, Legré M, Minshull C, Sajeed S. Creation of backdoors in quantum communications via laser damage. Phys Rev A. 2016;94:030302. doi:10.1103/PhysRevA.94.030302.